



Cite this: DOI: 10.1039/d1ee00317h

Received 30th January 2021,
Accepted 16th March 2021

DOI: 10.1039/d1ee00317h

rsc.li/ees

A high-performance rocking-chair lithium-ion battery-supercapacitor hybrid device boosted by doubly matched capacity and kinetics of the faradaic electrodes†

Feng Su,^{‡ab} Jieqiong Qin,^{‡ac} Pratteek Das,^{ab} Feng Zhou^{ad} and
Zhong-Shuai Wu^{ib*ad}

Battery-supercapacitor hybrid devices (BSHDs) are promising for certain applications requiring both high energy and power densities, but restricted by the electrolyte-consuming mechanism and imbalance of charge-storage capacity and electrode kinetics between battery-type and capacitor-type electrodes. Herein, a new prototype of rocking-chair lithium-ion BSHD with high energy and power densities is developed by employing pseudocapacitive T-Nb₂O₅ with a porous nanoflower structure as the anode and battery-type LiNi_{0.815}Co_{0.15}Al_{0.035}O₂ complexed in a three-dimensional interconnected conductive network as the cathode. Benefiting from the rational selection and optimization of the active material and electrode architecture, the anode and cathode exhibit exceptionally matched faradaic capacity and kinetics. Consequently, the BSHD delivers superior performance (165 W h kg⁻¹ at 105 W kg⁻¹ and 9.1 kW kg⁻¹ at 83 W h kg⁻¹) to previously reported rocking-chair BSHDs and could surpass the state-of-the-art electrolyte-consuming BSHDs at the device level. Therefore, this work will open a new avenue towards high-performance BSHDs.

Broader context

The huge performance gap between batteries undergoing slow bulk redox reaction and supercapacitors involving rapid surface-controlled ion adsorption or redox reaction has stimulated the development of battery-supercapacitor hybrid devices (BSHDs). Combining battery-type and capacitor-type electrodes in one cell, these devices simultaneously inherit the merits of different charge storage mechanisms, fulfilling the dual demands for high energy and power densities. However, the performance of current BSHDs is highly restricted by the imbalance of charge-storage capacity and electrode kinetics between the two electrodes. Besides, most of the present BSHDs work with electrolyte-consuming mechanisms, where a large amount of electrolyte is needed to serve as an ion reservoir, enabling dramatically lowered energy density at the device level. Herein, we develop a new prototype of BSHDs based on two matched faradaic electrodes with a rocking-chair mechanism analogous to lithium-ion batteries. By virtue of doubly matched capacity and kinetics, the BSHD achieves superior performance to counterparts with unmatched electrodes. Moreover, the less demand for electrolyte endows the BSHD with a higher theoretical energy density compared with other electrolyte-consuming BSHDs. This work can inspire cell configuration design and electrode structure optimization for high-energy and high-power electrochemical energy storage.

Introduction

The rapid development of consumer electronics, electric vehicles and the Internet of Things requires versatile power sources with high energy density, high power density and multiple

functionalities.^{1–3} To this end, extensive research has been conducted on integrating energy storage devices with energy-harvesting (*e.g.*, solar cell, nanogenerator) and energy-consuming components (*e.g.*, sensor, actuator) to form highly integrated self-powered systems^{4–6} or constructing hybrid energy storage devices to gain a synergetic combination of properties of different energy storage mechanisms.^{7,8} As a typical example, battery-supercapacitor hybrid devices (BSHDs) combining battery-type and capacitor-type electrodes in one cell are proposed to bridge the performance gap between batteries with high energy density but sluggish electrochemical kinetics and supercapacitors with rapid charge storage process yet limited energy density⁹ and to obtain both high energy density and power density from a single device.¹⁰

Although various BSHDs have shown the tradeoff between batteries and supercapacitors in several electrolytes containing

^a State Key Laboratory of Catalysis, Dalian Institute of Chemical Physics, Chinese Academy of Sciences, 457 Zhongshan Road, Dalian 116023, China. E-mail: wuzs@dicp.ac.cn

^b University of Chinese Academy of Sciences, 19 A Yuquan Rd, Shijingshan District, Beijing 100049, China

^c College of Science, Henan Agricultural University, No. 63 Agricultural Road, Zhengzhou 450002, China

^d Dalian National Laboratory for Clean Energy, Chinese Academy of Sciences, 457 Zhongshan Road, Dalian 116023, China

† Electronic supplementary information (ESI) available. See DOI: 10.1039/d1ee00317h

‡ These authors contributed equally to this work.

lithium ions, sodium ions and so on,^{11,12} the electrochemical performance is extremely restricted by the imbalance of charge-storage capacity and electrode kinetics between the two types of electrodes.^{8,10} As a result, the capacity or energy density is highly limited by the low-capacity capacitor-type electrode, and the rate capability or power density is primarily dependent on the low-rate battery-type electrode.^{8,10} The disparity of rate capability also imposes difficulties in determining the mass ratio of the two electrodes because the value corresponding to full utilization of the charge-storage capacities of the two electrodes is not the same at different charge/discharge rates.¹³ Until now, great efforts have been dedicated to designing nanostructured battery materials with high rate capability^{14–16} and modified porous carbon materials with high capacity,^{17–19} but this issue still hinders further performance improvement.

Another key point that should be taken into consideration is the working mechanism of BSHDs. So far, most nonaqueous BSHDs consist of a battery-type anode (*e.g.*, graphite, $\text{Li}_4\text{Ti}_5\text{O}_{12}$) and a capacitor-type cathode (*e.g.*, activated carbon (AC), graphene).^{20–22} This configuration works with the electrolyte-consuming mechanism, where the cations and anions supplied by the electrolyte move to the anode and cathode upon charging and go back to the electrolyte upon discharging.²³ Consequently, a large amount of electrolyte is required to ensure the proper functioning of these devices and prevent the increase of internal resistance due to the depletion of salts in the electrolyte, thus weighing down the energy density at the device level.^{23,24} In contrast, the rocking-chair mechanism that commonly exists in metal-ion batteries requires much less quantity of electrolyte because the active ions are released from the electrode during charge/discharge, and the electrolyte maintains a constant overall concentration.^{25,26} For BSHDs, the configuration composed of a capacitor-type anode (*e.g.*, AC, MXene) and a battery-type cathode (*e.g.*, LiFePO_4 , $\text{Na}_3\text{V}_2\text{O}_2(\text{PO}_4)_2\text{F}$) can realize an analogous operating principle.^{27–29} Nevertheless, rocking-chair-type BSHDs with double matching of capacity and rate capability between the anode and cathode is still challenging.

In this work, we demonstrate a new prototype of rocking-chair BSHD with exceptional matching of charge-storage capacity and balancing of electrode kinetics between the pseudocapacitive $\text{T-Nb}_2\text{O}_5$ anode and battery-type nickel-rich layered oxide ($\text{LiNi}_{0.815}\text{Co}_{0.15}\text{Al}_{0.035}\text{O}_2$, NCA) cathode, working in nonaqueous lithium-ion-containing electrolyte. The two faradaic electrodes of $\text{T-Nb}_2\text{O}_5$ and NCA possess comparable capacities, *e.g.* 175 and 169 mA h g^{-1} at 0.1 A g^{-1} , both of which are much higher than that of commonly used AC with electric double-layer (EDL) charge storage behavior ($\sim 35 \text{ mA h g}^{-1}$ within the potential range of 3–4.5 V or 1.5–3 V vs. Li^+/Li).³⁰ For electrode kinetics matching, battery-type NCA microspheres are fully integrated into a three-dimensional (3D) interconnected conductive network (NCA-3D) formed by two-dimensional (2D) electrochemically exfoliated graphene (EG) sheets, one-dimensional (1D) carbon nanotubes (CNTs) and conductive polymer binder (poly(3-hexylthiophene-2,5-diyl), P3HT), which greatly reduces the resistance and polarization during charge/discharge and thus improves the

high-rate charge-storage capability of NCA. Besides, the porous nanoflower structure of $\text{T-Nb}_2\text{O}_5$ ($\text{T-Nb}_2\text{O}_5\text{-NF}$) can further facilitate fast lithium-ion transport in the electrode. As a consequence, the anode and cathode exhibit similar rate capability, *e.g.* 130 and 116 mA h g^{-1} retained at 5 A g^{-1} . Based on the above two matched faradaic electrodes, the assembled $\text{T-Nb}_2\text{O}_5\text{-NF}/\text{NCA}$ -3D BSHD achieves both high energy density of 165 W h kg^{-1} at 105 W kg^{-1} and high power density of 9.1 kW kg^{-1} at 83 W h kg^{-1} , outperforming previously reported rocking-chair BSHDs.

Results and discussion

The configuration of the rocking-chair BSHD is schematically illustrated in Fig. 1a. $\text{T-Nb}_2\text{O}_5$ is selected as the anode material due to its intercalation pseudocapacitive charge storage behavior, which exhibits higher capacity originating from faradaic insertion of lithium ions yet similarly rapid kinetics compared to EDL capacitors.³¹ Additionally, operated in a safe potential window of 1–3 V vs. Li^+/Li (Fig. 1b), $\text{T-Nb}_2\text{O}_5$ can be prepared into various nanostructures without suffering from severe side reactions³² and does not require a prelithiation process for full cell assembly.³³ Meanwhile, nickel-rich NCA is employed as the battery-type cathode material owing to its high voltage and capacity (Fig. 1b), which can compensate for the relatively high working potential of $\text{T-Nb}_2\text{O}_5$ and endow the full cell with high energy density. Also, the layer structured NCA has shown potential for high-rate charge/discharge after structure modification.^{34,35} Furthermore, the substitution of faradaic electrodes for AC, which is commonly employed as a cathode for electrolyte-consuming BSHDs (*e.g.*, $\text{Nb}_2\text{O}_5//\text{AC}$) and an anode for rocking-chair BSHDs (*e.g.*, $\text{AC}/\text{LiNi}_{0.5}\text{Mn}_{1.5}\text{O}_5$), promises higher capacity and energy density for the full cell. During charging, lithium ions are released from the NCA cathode and insert into the $\text{T-Nb}_2\text{O}_5$ anode. A reverse process occurs upon discharging. It is noted that different from the electrolyte-consuming BSHDs where the electrolyte serves as an ion reservoir and should be regarded as an active material (Fig. 1c), the required lithium ions in the rocking-chair cell can be provided by the electrode, and the electrolyte only serves as a transport medium.²³ Considering the moderate capacity of electrolyte salts (*e.g.*, 176 mA h g^{-1} for LiPF_6) and the weight of required solvents, the reduced demand for electrolyte of this rocking-chair cell would enable a substantially higher conversion ratio of energy/power density from the electrode material to the whole device.^{26,36} Fig. 1d presents typical galvanostatic charge/discharge (GCD) profiles of $\text{T-Nb}_2\text{O}_5$ and NCA. Given the comparable capacities, the remaining challenge is how to balance the electrode kinetics. To achieve this goal, a well-designed regulation of active material and electrode architecture has been conducted to facilitate the charge transfer processes.

$\text{T-Nb}_2\text{O}_5\text{-NF}$ for the anode was prepared by a solvothermal method, followed by calcination for the transformation of the crystalline phase (see details in the Experimental, ESI†). The X-ray powder diffraction (XRD) pattern of the calcinated sample well matches that of the orthorhombic phase of Nb_2O_5 (JPCDS No. 30-0873, Fig. 2a). The crystalline structure is also confirmed

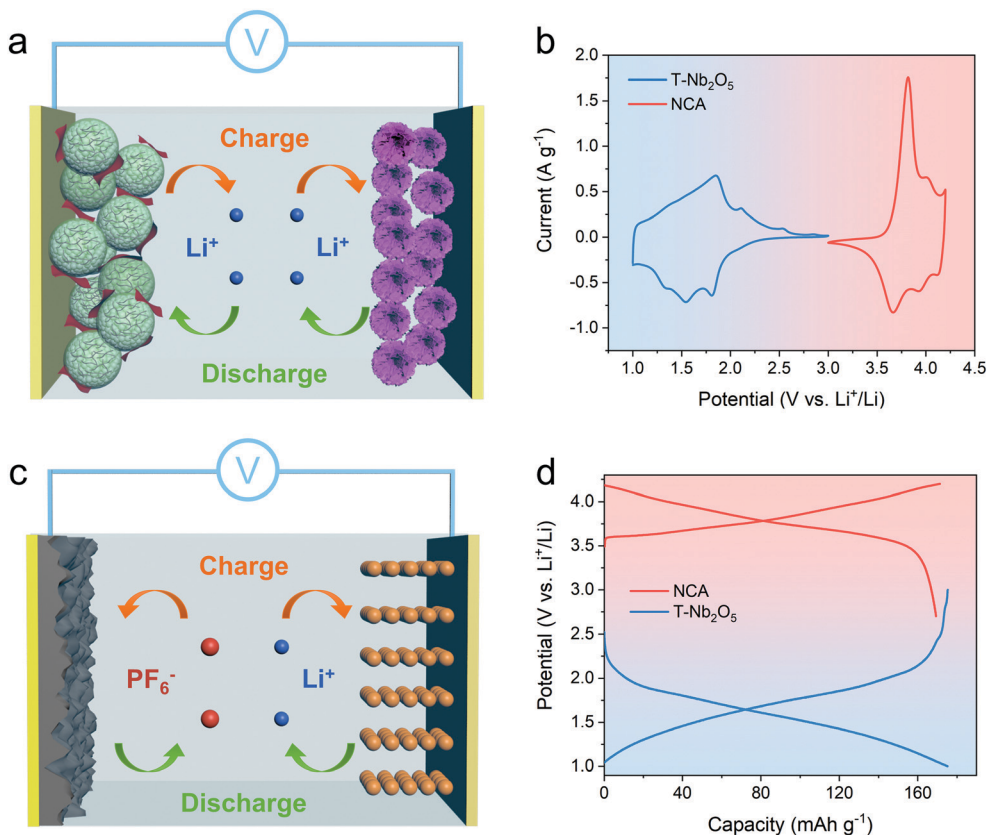


Fig. 1 (a) Schematic illustration of the charge storage mechanism for rocking-chair T-Nb₂O₅-NF//NCA-3D BSHD. (b) Typical CV curves of T-Nb₂O₅ and NCA at 0.8 mV s⁻¹. (c) Schematic illustration of the charge storage mechanism for electrolyte-consuming BSHDs. (d) Typical GCD profiles of T-Nb₂O₅ and NCA at 0.1 A g⁻¹.

by the Raman spectrum (Fig. S1, ESI[†]), which exhibits the characteristic bands at 120, 227, 309 and 689 cm⁻¹, and the high-resolution transition electron microscopy (HRTEM) image (Fig. S2a, ESI[†]), which displays a lattice spacing of 0.30 nm, corresponding to the crystalline plane (180) of the orthorhombic phase.^{15,37} A good crystallization ensures the favored crystallographic pathways for fast diffusion of lithium ions.³⁷ From scanning electron microscopy (SEM) images, it is observed that the as-synthesized niobium oxide exhibits a well-defined nanoflower structure assembled by interconnected smooth thin nanosheets (Fig. 2b and Fig. S2b, ESI[†]). Elemental mapping images (Fig. S2c, ESI[†]) clearly reveal the homogeneous distribution of Nb and O in the nanosheets. After calcination treatment, the nanoflower assembly is maintained, while the nanosheets possess a more porous structure (Fig. 2c, d and Fig. S2d, e, ESI[†]). Such porous nanoflower structure can provide open channels that facilitate electrolyte infiltration and ion transport (Fig. 2e).^{15,38}

Although nanostructuring has been extensively demonstrated to boost ion diffusion and electrode kinetics, it may be unsuitable for high-voltage NCA because the increased surface area can cause several new issues, such as the inactive surface layer of improperly mixed cations and unstable electrode/electrolyte interface, which would lower the charge storage capacity and aggravate the structure degradation of the high-surface-area

systems.^{38,39} To address this issue, we designed a 3D interconnected conductive network composed of 2D EG sheets (Fig. S3 and S4, ESI[†]), 1D CNTs and conductive P3HT binder (mass ratio of NCA : EG : CNT : P3HT is 90 : 4 : 3 : 3; see details in the Experimental, ESI[†]), all of which work together to synergistically reduce the resistance and polarization (Fig. 2f) and thereby accelerate the charge transfer process of the NCA cathode. Fig. 2g displays the XRD pattern of pristine NCA. It is validated that all diffraction peaks are well indexed to the hexagonal α -NaFeO₂ structure without obvious impurity phase, and the splitting of (006)/(102) and (108)/(110) peaks indicates a highly ordered layered structure.³⁵ SEM images show that the pristine sample consists of micron-sized spherical secondary agglomerates formed by small primary particles (Fig. S5, ESI[†]). As shown in Fig. 2h and i, the CNTs distribute evenly on the surface of the NCA microspheres, affording short-range electronic conductivity; meanwhile, the 2D EG sheets can provide a fast planar conductive path between the NCA particles.^{40,41} The CNTs also offer *meso*-porosity to promote electrolyte penetration and ion transport throughout the electrode.⁴² Besides, the electronic conductivity of the entire electrode is further improved by the use of the P3HT binder, which is highly conductive after electrochemical doping.⁴³ Notably, the cyclic voltammetry (CV) curve of P3HT with two anodic peaks located at 3.33 and 3.73 V vs. Li⁺/Li indicates that the electrochemical

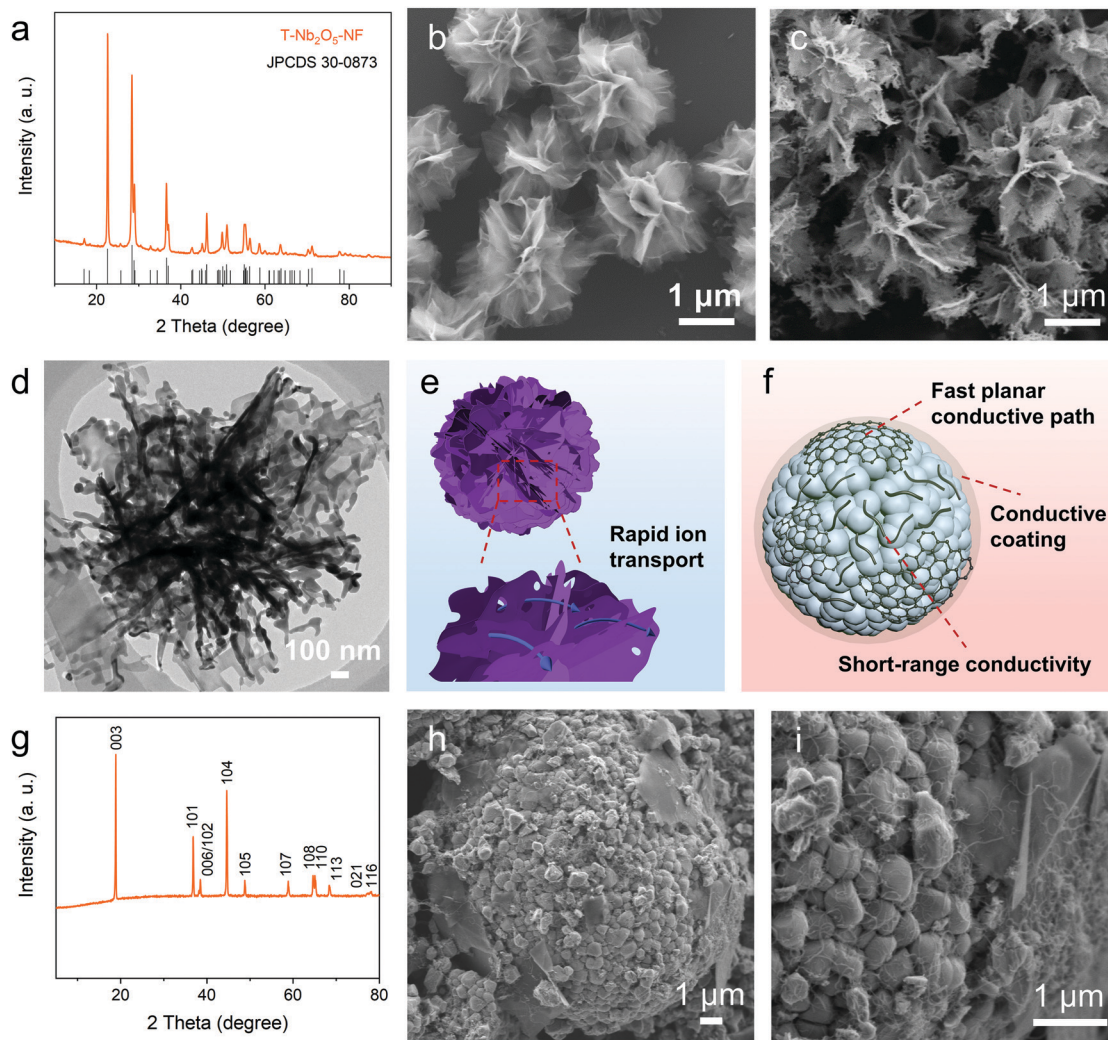


Fig. 2 Characterization of materials and electrodes. (a) XRD pattern, (b and c) SEM images and (d) TEM image of T-Nb₂O₅-NF. (e and f) Schematic illustration of the structures of (e) T-Nb₂O₅-NF and (f) NCA-3D. (g) XRD pattern of pristine NCA. (h and i) SEM images of the NCA-3D electrode.

doping processes can occur within the operating potential window of the NCA cathode (Fig. S6, ESI[†]). Moreover, the uniformly coated P3HT on NCA microspheres, as confirmed by elemental mapping images (Fig. S7, ESI[†]), can greatly reduce the electrode/electrolyte interface resistance by virtue of its good electronic and ionic conductivity and work as a protective layer that efficiently suppresses electrolyte breakdown on the surface of the NCA microspheres and stabilizes their structural integrity during long-term cycling.⁴⁴ In sharp contrast, the electronic conducting pathway in the conventional electrode (donated as NCA-C) with acetylene black additive and poly(vinylidene fluoride) binder is mainly formed by the point contact between the NCA microspheres and acetylene black particles (Fig. S8, ESI[†]), leading to an inefficient conducting network.

The electrochemical performance was measured using coin-type half cells with lithium foil as the counter and reference electrode and full cells with T-Nb₂O₅-NF as the anode and NCA as the cathode. It is noted that to avoid the experimental error from the inhomogeneity of electrodes and the misalignment between

the anode and cathode slices in full cells, at least three half or full cells with almost identical electrochemical performance were used to confirm the reproducibility (Fig. S9, ESI[†]). Fig. 3a shows the typical GCD profiles of T-Nb₂O₅-NF within a potential window of 1–3 V vs. Li⁺/Li, in which the linear region suggests the pseudo-capacitive behavior of T-Nb₂O₅.⁴⁵ Impressively, T-Nb₂O₅-NF delivers highly reversible capacities of 175 and 130 mA h g⁻¹ at current densities of 0.1 and 5 A g⁻¹ with a capacity retention of 74% (Fig. 3b). This remarkable rate capability is among the best results reported for Nb-based oxides (Table S1, ESI[†]). Moreover, T-Nb₂O₅-NF also exhibits excellent structural stability with a high capacity of 129 mA h g⁻¹ maintained after 400 cycles at 1 A g⁻¹ (Fig. S10, ESI[†]).

To further understand the lithium-ion storage behavior of T-Nb₂O₅-NF, a kinetics study based on CV curves (Fig. 3c) was performed using the following equation:⁴⁶

$$Q(\nu) = Q_{\text{capacitive}} + k\nu^{-1/2}$$

where the total charge storage capacity (Q) of a material is considered to be composed of two contributions from

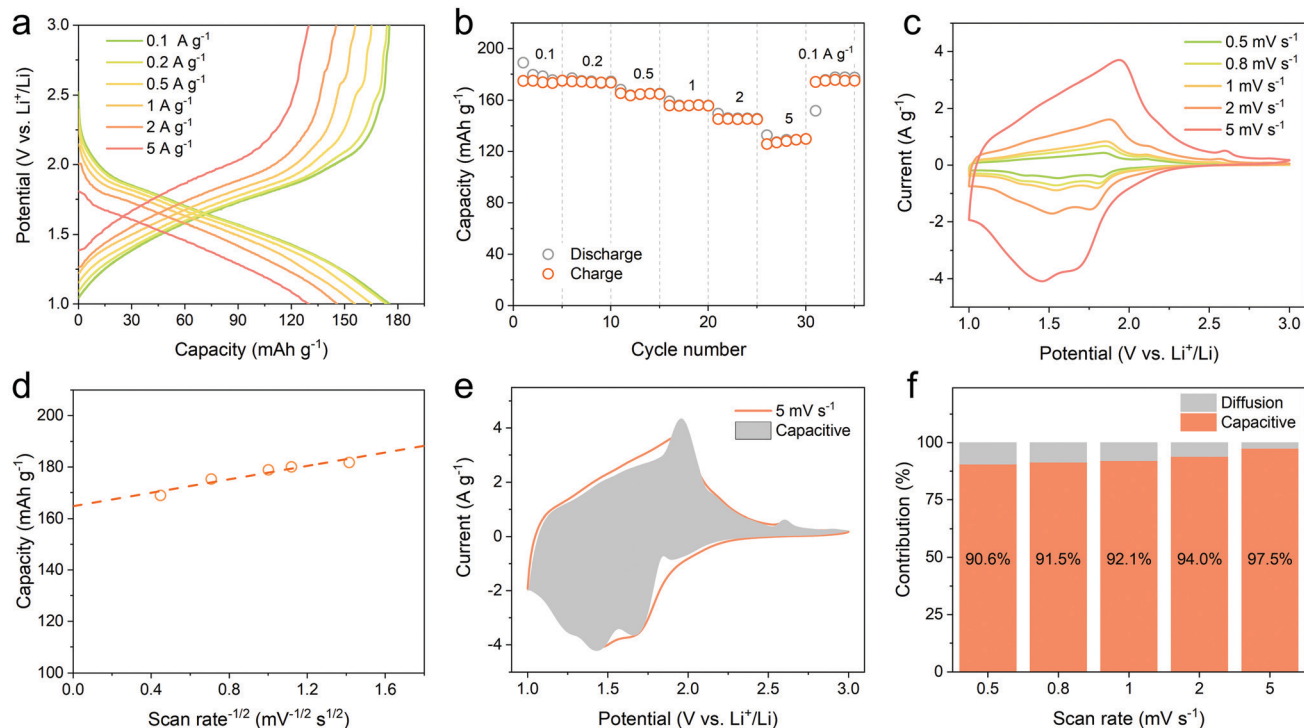


Fig. 3 Electrochemical performance and electrode kinetics of the T-Nb₂O₅-NF anode. (a) GCD profiles at different current densities. (b) Rate performance. (c) CV curves at various scan rates. (d) Voltammetric capacity as a function of scan rate^{-1/2}. (e) Capacitive current response (grey) at 5 mV s⁻¹. (f) Normalized contribution of capacitive and diffusion-controlled charge storage at different scan rates.

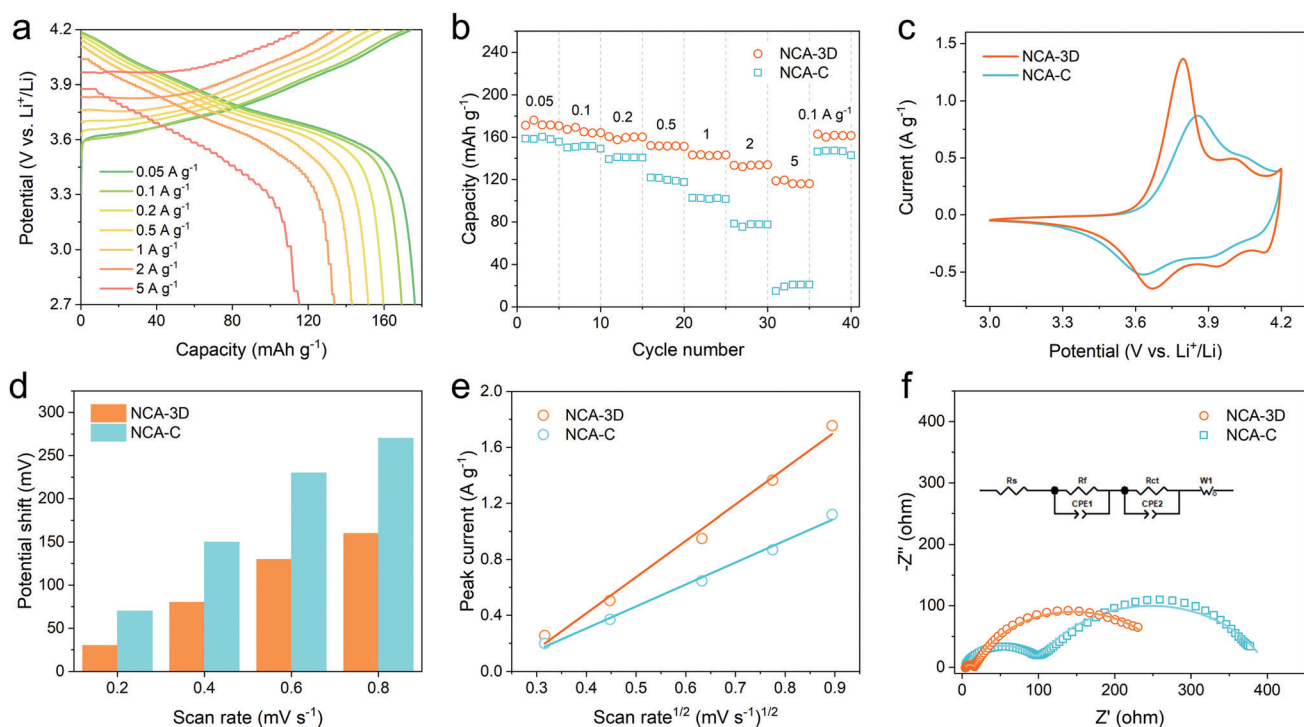


Fig. 4 Electrochemical performance and electrode kinetics of the NCA-3D and NCA-C cathodes. (a) GCD profiles of NCA-3D. (b) Rate performance of NCA-3D and NCA-C. (c) CV curves of different electrodes at 0.6 mV s⁻¹. (d) Potential shift between anodic and cathodic peaks in the CV curves as a function of scan rate. (e) Anodic peak current as a function of scan rate^{1/2}. (f) Nyquist plots of different electrodes at 3.6 V vs. Li⁺/Li.

capacitive behaviors ($Q_{\text{capacitive}}$) and diffusion-controlled bulk processes ($k\nu^{-1/2}$); ν is the sweep rate. According to this equation, when $\nu = \infty$, the intercept of the extrapolated Q versus $\nu^{-1/2}$ linear trend line (Fig. 3d) represents the capacitive charge storage capacity ($Q_{\text{capacitive}}$), which is calculated to be 165 mA h g^{-1} . The capacitive current response as a function of potential was also extracted by separating the total current into capacitive ($k_1\nu$) and diffusion-controlled ($k_2\nu^{1/2}$) components (Fig. 3e).³¹ Fig. 3f presents the corresponding capacitive contribution at different sweep rates. It is revealed that more than 90% of the total capacity originates from capacitive charge storage, giving rise to high rate capability.

To confirm the advantages of the 3D interconnected conductive network, GCD measurements were conducted to compare the rate capability between NCA-3D and NCA-C electrodes (Fig. 4a and Fig. S11, ESI[†]). It can be seen that NCA-3D delivers a higher capacity of 176 mA h g^{-1} compared with NCA-C (160 mA h g^{-1}) at 0.05 A g^{-1} . With stepwise increased current densities, the difference dramatically increases (Fig. 4b). Notably, NCA-3D still provides 116 mA h g^{-1} at a high current density of 5 A g^{-1} , which is more than five times as large as that of NCA-C (21 mA h g^{-1}) and exceeds most reported values for nickel-rich layered oxide materials (Table S2, ESI[†]). Moreover, NCA-3D exhibits quite a stable cyclability with a retention of 90% after 200 cycles, while NCA-C displays continuous capacity fading and retains only 65% of the initial capacity (Fig. S12, ESI[†]). Such an enhancement of cyclability is ascribed to the surface coating by P3HT and EG, which can effectively protect NCA from electrolyte breakdown and mitigate structure degradation.⁴⁴

Furthermore, CV curves were measured to figure out the influence of the 3D interconnected conductive network on electrode kinetics (Fig. S13, ESI[†]). The potential shifts (ΔE) between the oxidation and reduction peaks of the CV curves are in close association with the electrochemical polarization accompanied by the extraction and insertion of lithium ions. As presented in Fig. 4c, the anodic and cathodic peaks at 0.6 mV s^{-1} are located at 3.80 V and 3.67 V ($\Delta E = 0.13$ V) for NCA-3D, compared to 3.86 V and 3.63 V ($\Delta E = 0.23$ V) for NCA-C. The smaller potential shifts of NCA-3D (Fig. 4d) reveal significantly reduced polarization during charge/discharge. Fig. 4e and Fig. S14 (ESI[†]) show the linear relationship between the peak current (I_p) and the square root of sweep rate ($\nu^{1/2}$). It is well recognized that the apparent diffusion coefficient of lithium ions is proportional to the slope of the I_p versus $\nu^{1/2}$ trend line.⁴⁷ As expected, the trend line for NCA-3D shows a larger slope, suggestive of the enhanced lithium-ion migration behavior. Besides, electrochemical impedance spectroscopy (EIS) was adopted to compare the resistance of different electrodes (Fig. 4f), in which the first semicircle at high frequency is related to the interface film resistance (R_f) and the second semicircle represents the charge transfer resistance (R_{ct}).⁴⁸ Owing to the synergy of the 3D conductive network comprising EG sheets, CNTs and P3HT, NCA-3D displays both lower R_f (11 Ω) and R_{ct} (261 Ω) than NCA-C (92 Ω and 303 Ω). Therefore, it is demonstrated that the 3D interconnected

conductive network plays a critical role in reducing the resistance and polarization during charge/discharge.

Thanks to the above rational selection of active materials and elaborated design of electrode architecture, the exceptional matching of capacity and balancing of rate capability between the capacitor-type and battery-type electrodes were substantially obtained through employing the T-Nb₂O₅-NF anode and NCA-3D cathode (Fig. 5a). To fabricate full BSHDs, the mass ratio of active materials between the cathode and anode was first determined to be ~1:1 according to the comparable capacities of the cathode and anode to maximize the energy density of the full cell, as shown in Fig. S15 (ESI[†]). Furthermore, GCD measurements with different voltage ranges were carried out to optimize the voltage window of the full cell (Fig. S16a, ESI[†]). Higher capacity and energy density can be obtained within a wider voltage range of 0.5–3.2 V (Fig. S16b and c, ESI[†]), but such an excessive depth of charge/discharge results in low cycling stability (Fig. S16d, ESI[†]). Therefore, an appropriate operating voltage of 0.8–3.0 V was adopted to reach a trade-off between energy density and cycle life. In addition, a three-electrode GCD measurement using Ag wire as a quasi-reference electrode was conducted to provide a full image of the BSHD (Fig. S17, ESI[†]). As shown in Fig. 5b, the potential swing ranges of the cathode and anode at 0.1 A g^{-1} are 0.38–1.11 V and –0.42 to –1.89 V vs. Ag quasi-reference, respectively, which are included in the redox-active potential ranges of these two electrodes. Benefiting from the balanced electrode kinetics, the potential swing range of the cathode shifts slightly to 0.14–1.19 V and 0.01–1.23 V vs. Ag quasi-reference at high current densities of 1 A g^{-1} and 2 A g^{-1} , respectively (Fig. S18, ESI[†]).

Fig. 5c shows the first three GCD cycles of the as-assembled T-Nb₂O₅-NF//NCA-3D BSHD at 0.05 A g^{-1} , which displays an initial coulombic efficiency of 80%, and quickly becomes stable upon the second cycle with an average discharge voltage of 2.1 V. The CV curves show a couple of broad peaks (Fig. 5d), which is a typical feature for BSHDs. To examine the electrochemical kinetics, the b -value was calculated according to the power-law relationship ($I = a\nu^b$), where it corresponds to the slope of the $\log I$ versus $\log \nu$ trend line (Fig. 5e). Notably, the b -values are 0.96 for the anodic peak and 0.89 for the cathodic peak. The high b -value (Fig. S19, ESI[†]) indicates a mixed charge storage behavior with a dominant surface-controlled pseudo-capacitive contribution, which suggests highly rapid electrochemical kinetics.⁴⁸ As expected, the BSHD delivers a capacity of 78 mA h g^{-1} at 0.05 A g^{-1} and retains 58% of the capacity even at a high current density of 5 A g^{-1} (Fig. 5f and Fig. S20, ESI[†]), showing outstanding rate capability. Moreover, the cyclability of BSHD was evaluated at a current density of 1 A g^{-1} , and 91% of the initial capacity is maintained after 400 cycles, accompanied by an excellent coulombic efficiency of ~100% (Fig. 5g).

To validate the applicability of T-Nb₂O₅-NF//NCA-3D BSHD as a power source, the energy and power densities based on the total mass of active materials in the two electrodes were calculated from the GCD profiles. Impressively, T-Nb₂O₅-NF//NCA-3D BSHD achieves an energy density of 165 W h kg^{-1} at

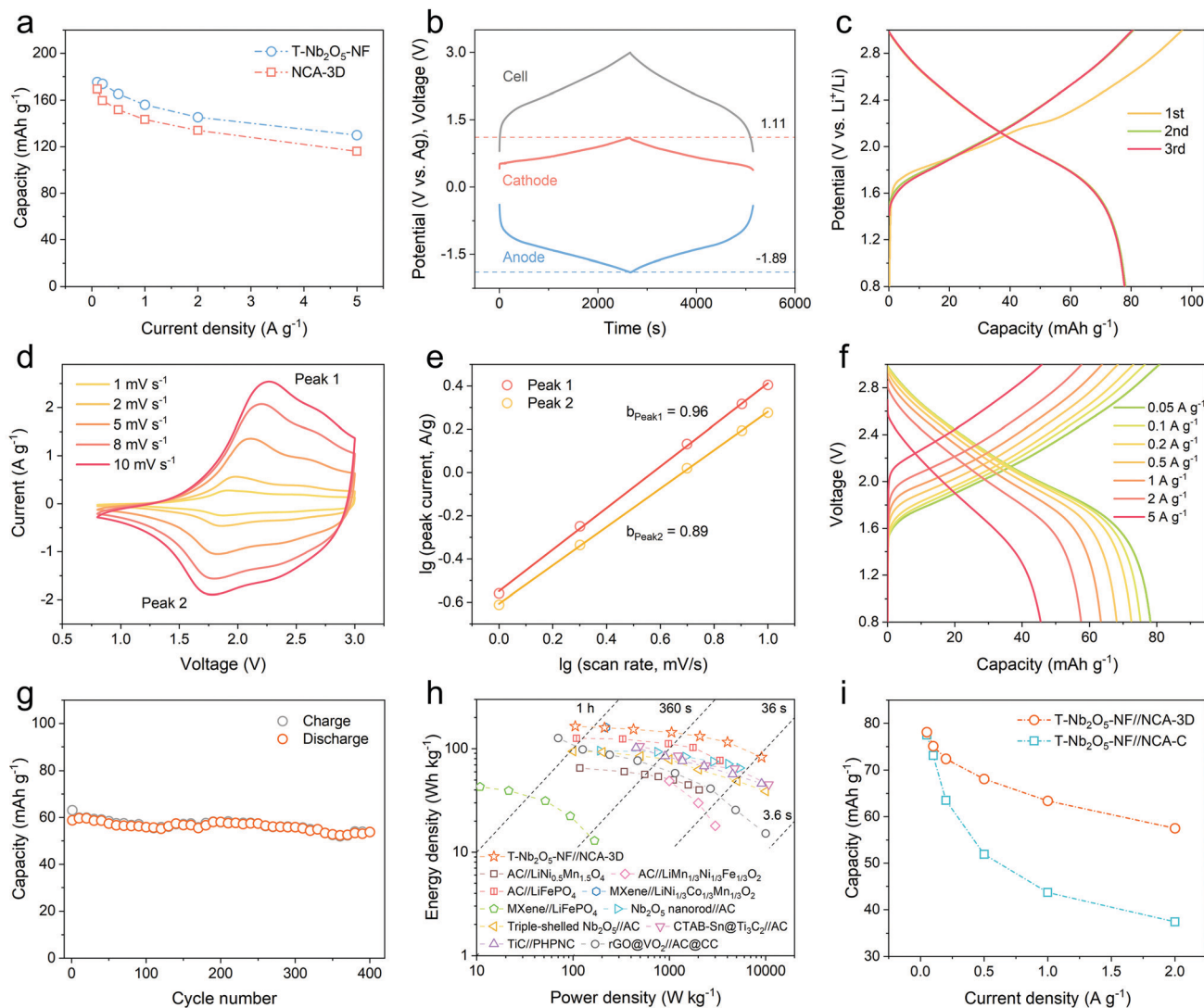


Fig. 5 Electrochemical performance of the T-Nb₂O₅-NF//NCA-3D BSHD. (a) Capacity as a function of current density for the T-Nb₂O₅-NF anode and NCA-3D cathode. (b) Potential profiles of the anode, cathode and full cell obtained from the three-electrode GCD measurement at 0.1 A g⁻¹. (c) Initial three GCD cycles of T-Nb₂O₅-NF//NCA-3D BSHD at 0.05 A g⁻¹. (d) CV curves of T-Nb₂O₅-NF//NCA-3D BSHD at various scan rates. (e) Linear relationship between log of peak current (log *I*_p) and log of scan rate (log *v*). (f) GCD profiles of T-Nb₂O₅-NF//NCA-3D BSHD at different current densities. (g) Cycling stability of T-Nb₂O₅-NF//NCA-3D BSHD at 1 A g⁻¹. (h) Ragone plot of T-Nb₂O₅-NF//NCA-3D BSHD in comparison with those of the reported BSHDs. (i) Rate performance of T-Nb₂O₅-NF//NCA-3D and T-Nb₂O₅-NF//NCA-C BSHDs.

105 W kg⁻¹ and a power density of 9.1 kW kg⁻¹ at 83 W h kg⁻¹ (Fig. 5h). It is noteworthy that the charge/discharge time of the latter is only ~33 s (Fig. S21, ESI[†]). Such remarkable energy and power densities are superior to those of previously reported rocking-chair BSHDs, such as AC//LiNi_{0.5}Mn_{1.5}O₄ (50 W h kg⁻¹ at 1.1 kW kg⁻¹),⁴⁹ AC//LiMn_{1/3}Ni_{1/3}Fe_{1/3}O₂ (49 W h kg⁻¹ at 1 kW kg⁻¹ and 3 kW kg⁻¹ at 18 W h kg⁻¹),⁵⁰ AC//LiFePO₄ (126 W h kg⁻¹ at 109 W kg⁻¹ and 3.4 kW kg⁻¹ at 77 W h kg⁻¹),²⁸ MXene//LiFePO₄ (43 W h kg⁻¹)⁵¹ and MXene//LiNi_{1/3}Co_{1/3}Mn_{1/3}O₂ (160 W h kg⁻¹ at 220 W kg⁻¹)²⁷ (Fig. 5h and Table S3, ESI[†]). For comparison, T-Nb₂O₅-NF//NCA-C full cells were also measured (Fig. S22a, ESI[†]). By virtue of the balanced electrode kinetics, T-Nb₂O₅-NF//NCA-3D BSHD exhibits greatly enhanced rate capability and power density (Fig. 5i and Fig. S22b, ESI[†]). Besides, the present BSHD also provides improved energy density

compared with reported T-Nb₂O₅//AC cells (usually below 100 W h kg⁻¹)^{15,52} and other typical BSHDs with an EDL-type carbon cathode, such as CTAB-Sn@Ti₃C₂//AC (105.56 W h kg⁻¹),⁵³ TiC//Porous nitrogen-doped carbon (101.5 W h kg⁻¹)⁵⁴ and rGO@VO₂//AC (126.7 W h kg⁻¹)¹⁴ (Fig. 5h and Table S3, ESI[†]), which is benefited from the matched capacity through the substitution of high-capacity faradaic electrodes for EDL-type electrodes. Overall, the above results demonstrate the significance of double matching of charge-storage capacity and electrode kinetics between the anode and cathode. Furthermore, the theoretical energy density based on the electrode material and electrolyte was evaluated to highlight the superiority of the rocking-chair configuration, where the required minimum amount of electrolyte is determined by the pore volume of the electrodes for rocking-chair BSHDs and by the charge balance between the

electrodes and electrolyte for electrolyte-consuming BSHDs. The estimated energy density of the as-fabricated T-Nb₂O₅-NF//NCA-3D BSHD, normalized by the mass of active materials and the minimum amount of electrolyte, is as high as $\sim 80 \text{ W h kg}^{-1}$, which is comparable and even superior to those of the state-of-the-art electrolyte-consuming BSHDs (calculation details presented in ESI,† Note and Fig. S23).

Conclusions

In summary, a rocking-chair lithium-ion BSHD delivering high energy and power densities *via* two faradaic electrodes with highly matched capacity and balanced kinetics has been constructed by combining a high-capacity pseudocapacitive T-Nb₂O₅-NF anode with a fast lithium-ion intercalation path and high-rate battery-type NCA-3D cathode with an efficient conductive network. As a consequence, the as-assembled BSHD achieves a remarkable energy density of 165 W h kg^{-1} , while providing 83 W h kg^{-1} within an extremely short charge/discharge time of 33 s, outperforming previously reported rocking-chair BSHDs. Moreover, the less demand for electrolytes could endow the BSHD with superior energy density at the device level compared with the state-of-the-art electrolyte-consuming BSHDs. Therefore, this work demonstrates the importance of the rocking-chair configuration and double matching of charge-storage capacity and electrode kinetics. The proposed strategy will pave the way to next-generation high-energy and high-power BSHDs.

Conflicts of interest

There are no conflicts to declare.

Acknowledgements

This work was financially supported by the National Natural Science Foundation of China (Grants 51872283, 21805273, 22075279, 22005297, 22005298), National Key R&D Program of China (Grants 2016YFB0100100, 2016YFA0200200), Liaoning BaiQianWan Talents Program, Liaoning Revitalization Talents Program (Grant XLYC1807153), Natural Science Foundation of Liaoning Province, Joint Research Fund Liaoning-Shenyang National Laboratory for Materials Science (Grant 20180510038), Dalian Innovation Support Plan for High Level Talents (2019RT09), DICP (DICP ZZBS201708, DICP ZZBS201802, DICP I202032), DICP&QIBEBT (Grant DICP&QIBEBT UN201702), and DNL Cooperation Fund, CAS (DNL180310, DNL180308, DNL201912, DNL201915).

References

- 1 Y. E. Durmus, H. Zhang, F. Baakes, G. Desmaizieres, H. Hayun, L. Yang, M. Kolek, V. Küpers, J. Janek, D. Mandler, S. Passerini and Y. Ein-Eli, *Adv. Energy Mater.*, 2020, **10**, 2000089.
- 2 P. Simon and Y. Gogotsi, *Nat. Mater.*, 2020, **19**, 1151–1163.
- 3 X. Ji, *Energy Environ. Sci.*, 2019, **12**, 3203–3224.
- 4 S. Zheng, H. Wang, P. Das, Y. Zhang, Y. Cao, J. Ma, S. Liu and Z.-S. Wu, *Adv. Mater.*, 2021, **33**, 2005449.
- 5 A. Scalia, F. Bella, A. Lamberti, C. Gerbaldi and E. Tresso, *Energy*, 2019, **166**, 789–795.
- 6 A. Pedico, A. Lamberti, A. Gigot, M. Fontana, F. Bella, P. Rivolo, M. Cocuzza and C. F. Pirri, *ACS Appl. Energy Mater.*, 2018, **1**, 4440–4447.
- 7 D. P. Dubal, O. Ayyad, V. Ruiz and P. Gomez-Romero, *Chem. Soc. Rev.*, 2015, **44**, 1777–1790.
- 8 D. Tie, S. Huang, J. Wang, J. Ma, J. Zhang and Y. Zhao, *Energy Storage Mater.*, 2019, **21**, 22–40.
- 9 A. Noori, M. F. El-Kady, M. S. Rahmanifar, R. B. Kaner and M. F. Mousavi, *Chem. Soc. Rev.*, 2019, **48**, 1272–1341.
- 10 W. Zuo, R. Li, C. Zhou, Y. Li, J. Xia and J. Liu, *Adv. Sci.*, 2017, **4**, 1600539.
- 11 J. Ding, W. Hu, E. Paek and D. Mitlin, *Chem. Rev.*, 2018, **118**, 6457–6498.
- 12 H. Wang, C. Zhu, D. Chao, Q. Yan and H. J. Fan, *Adv. Mater.*, 2017, **29**, 1702093.
- 13 W. G. Pell and B. E. Conway, *J. Power Sources*, 2004, **136**, 334–345.
- 14 R. Sahoo, T. H. Lee, P. Duy Tho, L. Thi Hoai Thuong and Y. H. Lee, *ACS Nano*, 2019, **13**, 10776–10786.
- 15 R. Bi, N. Xu, H. Ren, N. Yang, Y. Sun, A. Cao, R. Yu and D. Wang, *Angew. Chem., Int. Ed.*, 2020, **59**, 4865–4868.
- 16 S. Zheng, S. Wang, Y. Dong, F. Zhou, J. Qin, X. Wang, F. Su, C. Sun, Z.-S. Wu, H.-M. Cheng and X. Bao, *Adv. Sci.*, 2019, **6**, 1902147.
- 17 Q. Xia, H. Yang, M. Wang, M. Yang, Q. Guo, L. Wan, H. Xia and Y. Yu, *Adv. Energy Mater.*, 2017, **7**, 1701336.
- 18 C. Li, X. Zhang, K. Wang, X. Sun and Y. Ma, *Carbon*, 2018, **140**, 237–248.
- 19 X. Hu, G. Zhong, J. Li, Y. Liu, J. Yuan, J. Chen, H. Zhan and Z. Wen, *Energy Environ. Sci.*, 2020, **13**, 2431–2440.
- 20 S. Zheng, J. Ma, Z.-S. Wu, F. Zhou, Y.-B. He, F. Kang, H.-M. Cheng and X. Bao, *Energy Environ. Sci.*, 2018, **11**, 2001–2009.
- 21 D. Han, Z. Weng, P. Li, Y. Tao, C. Cui, L. Zhang, W. Lin, Y. Gao, D. Kong and Q.-H. Yang, *Energy Storage Mater.*, 2019, **18**, 133–138.
- 22 L. Jin, X. Guo, R. Gong, J. Zheng, Z. Xiang, C. Zhang and J. P. Zheng, *Energy Storage Mater.*, 2019, **23**, 409–417.
- 23 B. Li, J. Zheng, H. Zhang, L. Jin, D. Yang, H. Lv, C. Shen, A. Shellikeri, Y. Zheng, R. Gong, J. P. Zheng and C. Zhang, *Adv. Mater.*, 2018, **30**, 1705670.
- 24 J. P. Zheng, *J. Electrochem. Soc.*, 2003, **150**, A484–A492.
- 25 H. D. Yoo, S.-D. Han, R. D. Bayliss, A. A. Gewirth, B. Genorio, N. N. Rajput, K. A. Persson, A. K. Burrell and J. Cabana, *ACS Appl. Mater. Interfaces*, 2016, **8**, 30853–30862.
- 26 J. P. Zheng, *J. Electrochem. Soc.*, 2009, **156**, A500–A505.
- 27 S. Kajiyama, L. Szabova, H. Iinuma, A. Sugahara, K. Gotoh, K. Sodeyama, Y. Tateyama, M. Okubo and A. Yamada, *Adv. Energy Mater.*, 2017, **7**, 1601873.
- 28 Y. Zhang, Z. Zhang, Y. Tang, D. Jia, Y. Huang, W. Pang, Z. Guo and Z. Zhou, *Adv. Funct. Mater.*, 2019, **29**, 1807895.

- 29 L. Wu, S. Dong, G. Pang, H. Li, C. Xu, Y. Zhang, H. Dou and X. Zhang, *J. Mater. Chem. A*, 2019, **7**, 1030–1037.
- 30 G. Li, Z. Yang, Z. Yin, H. Guo, Z. Wang, G. Yan, Y. Liu, L. Li and J. Wang, *J. Mater. Chem. A*, 2019, **7**, 15541–15563.
- 31 V. Augustyn, J. Come, M. A. Lowe, J. W. Kim, P.-L. Taberna, S. H. Tolbert, H. D. Abruna, P. Simon and B. Dunn, *Nat. Mater.*, 2013, **12**, 518–522.
- 32 J. Come, V. Augustyn, J. W. Kim, P. Rozier, P.-L. Taberna, P. Gogotsi, J. W. Long, B. Dunn and P. Simon, *J. Electrochem. Soc.*, 2014, **161**, A718–A725.
- 33 L. Jin, C. Shen, A. Shellikeri, Q. Wu, J. Zheng, P. Andrei, J.-G. Zhang and J. P. Zheng, *Energy Environ. Sci.*, 2020, **13**, 2341–2362.
- 34 B. Babu, P. Simon and A. Balducci, *Adv. Energy Mater.*, 2020, **10**, 2001128.
- 35 Y. Li, H. Yu, Y. Hu, H. Jiang and C. Li, *J. Energy Chem.*, 2018, **27**, 559–564.
- 36 J. P. Zheng, *J. Electrochem. Soc.*, 2005, **152**, A1864–A1869.
- 37 J. W. Kim, V. Augustyn and B. Dunn, *Adv. Energy Mater.*, 2012, **2**, 141–148.
- 38 B. K. Lesel, J. B. Cook, Y. Yan, T. C. Lin and S. H. Tolbert, *ACS Energy Lett.*, 2017, **2**, 2293–2298.
- 39 S. Hwang, W. Chang, S. M. Kim, D. Su, D. H. Kim, J. Y. Lee, K. Y. Chung and E. A. Stach, *Chem. Mater.*, 2014, **26**, 1084–1092.
- 40 L. T. Xu, W. Lv, K. Shi, S. J. Xiao, C. H. You, Y. B. He, F. Y. Kang and Q.-H. Yang, *Carbon*, 2019, **149**, 257–262.
- 41 F. Su and Z.-S. Wu, *J. Energy Chem.*, 2021, **53**, 354–357.
- 42 Y. Sun, J. Tang, F. Qin, J. Yuan, K. Zhang, J. Li, D.-M. Zhu and L.-C. Qin, *J. Mater. Chem. A*, 2017, **5**, 13601–13609.
- 43 S. L. Wu, A. E. Javier, D. Devaux, N. P. Balsara and V. Srinivasan, *J. Electrochem. Soc.*, 2014, **161**, A1836–A1843.
- 44 C.-H. Lai, D. S. Ashby, T. C. Lin, J. Lau, A. Dawson, S. H. Tolbert and B. S. Dunn, *Chem. Mater.*, 2018, **30**, 2589–2599.
- 45 C. Choi, D. S. Ashby, D. M. Butts, R. H. DeBlock, Q. Wei, J. Lau and B. Dunn, *Nat. Rev. Mater.*, 2020, **5**, 5–19.
- 46 S. Ardizzone, G. Fregonara and S. Trasatti, *Electrochim. Acta*, 1990, **35**, 263–267.
- 47 X. H. Rui, N. Yesibolati, S. R. Li, C. C. Yuan and C. H. Chen, *Solid State Ionics*, 2011, **187**, 58–63.
- 48 T. S. Mathis, N. Kurra, X. Wang, D. Pinto, P. Simon and Y. Gogotsi, *Adv. Energy Mater.*, 2019, **9**, 1902007.
- 49 A. Brandt, A. Balducci, U. Rodehorst, S. Menne, M. Winter and A. Bhaskar, *J. Electrochem. Soc.*, 2014, **161**, A1139–A1143.
- 50 K. Karthikeyan, S. Amaresh, V. Aravindan, H. Kim, K. S. Kang and Y. S. Lee, *J. Mater. Chem. A*, 2013, **1**, 707–714.
- 51 A. Byeon, A. M. Glushenkov, B. Anasori, P. Urbankowski, J. Li, B. W. Byles, B. Blake, K. L. Van Aken, S. Kota, E. Pomerantseva, J. W. Lee, Y. Chen and Y. Gogotsi, *J. Power Sources*, 2016, **326**, 686–694.
- 52 B. Deng, T. Lei, W. Zhu, L. Xiao and J. Liu, *Adv. Funct. Mater.*, 2018, **28**, 1704330.
- 53 J. Luo, W. Zhang, H. Yuan, C. Jin, L. Zhang, H. Huang, C. Liang, Y. Xia, J. Zhang, Y. Gan and X. Tao, *ACS Nano*, 2017, **11**, 2459–2469.
- 54 H. Wang, Y. Zhang, H. Ang, Y. Zhang, H. T. Tan, Y. Zhang, Y. Guo, J. B. Franklin, X. L. Wu, M. Srinivasan, H. J. Fan and Q. Yan, *Adv. Funct. Mater.*, 2016, **26**, 3082–3093.